Fluidization of epithelial sheets by active cell rearrangements

Matej Krajnc,[1,2,*] Sabyasachi Dasgupta,[3,4] Primož Ziherl,[2,5] and Jacques Prost[4,6]

[1]*Lewis-Sigler Institute for Integrative Genomics, Princeton University, Washington Road, Princeton, New Jersey USA, 08544*
[2]*Jožef Stefan Institute, Jamova 39, SI-1000, Ljubljana, Slovenia*
[3]*Department of Physics, University of Toronto, 60 St. George Street, Toronto, Ontario M5S 1A7, Canada*
[4]*Mechanobiology Institute, National University of Singapore, 5A Engineering Drive 1, Singapore 117411, Singapore*
[5]*Faculty of Mathematics and Physics, University of Ljubljana, Jadranska 19, SI-1000 Ljubljana, Slovenia*
[6]*Laboratoire Physico Chimie Curie, Institut Curie, PSL Research University, CNRS UMR168, 75005 Paris, France*

We theoretically explore fluidization of epithelial tissues by active T1 neighbor exchanges. We show that the geometry of cell-cell junctions encodes important information about the local features of the energy landscape, which we support by an elastic theory of T1 transformations. Using a 3D vertex model, we show that the degree of active noise driving forced cell rearrangements governs the stress-relaxation timescale of the tissue. We study tissue response to in-plane shear at different timescales. At short time, the tissue behaves as a solid, whereas its long-time fluid behavior can be associated with an effective viscosity which scales with the rate of active T1 transformations. Furthermore, we develop a coarse-grained theory, where we treat the tissue as an active fluid and confirm the results of the vertex model. The impact of cell rearrangements on tissue shape is illustrated by studying axial compression of an epithelial tube.

I. INTRODUCTION

In the early stages of animal development, many embryos consist of an epithelial sheet-like tissue which then deforms so as to form the various organs, the main morphogenetic modes relying on buckling, invagination, spreading, and in-plane migration. The three-dimensional (3D) tissue shapes resulting from these processes depend very much on the ability of cells to move within the tissue due to local stresses imposed by their neighbors [1,2], which is intrinsically associated with the energy barrier for cell rearrangement [3,4].

This motion is reminiscent of glassy dynamics [5,6] known from colloidal suspensions and granular materials [7]. One of its key features is the transition from the fluidlike state to a state characterized by a finite shear modulus. For example, in flat nonproliferating epithelia described by the 2D area- and perimeter-elasticity (APE) model [8,9], the energy barriers for cell rearrangements vanish at strong cell-cell adhesion or at weak contractility of the actomyosin belt [4]. In turn, intrinsically solid tissues can actively reorganize by oriented cell intercalations [10–13] or they can be fluidized by cell proliferation [8,14–16] and active cell motility [17–19]. These interesting findings raise the question whether nonproliferating solid tissues in which cells do not interact strongly with the substrate too can exhibit fluidlike behavior governed by, e.g., active remodeling of cell-cell junctions, and if yes, how such activity affects the overall 3D tissue shape. This could be especially important in the tissues of early embryos, which undergo extensive 3D shape transformations, driven almost exclusively by intra- and intercellular forces. Another important issue

concerns the reduced dimensionality of the 2D models, which provides valuable insight into the in-plane structure [8,9,20,21] and out-of-plane deformations of the tissue [22–28] yet leaves a lingering question of whether the approximations used are really justified.

To address these problems, we develop a theoretical model of the epithelial tissue, in which cells undergo active neighbor exchanges due to random nondirectional contractions of cell-cell junctions induced by, e.g., fluctuations of the junctional myosin. Combining this phenomenon with the recently proposed 3D vertex model (Fig. 1(a); [29–32]) allows us to construct a detailed computational representation of the tissue, which is then used to investigate the complex relationship between cell-scale activity and 3D tissue architecture. In particular, we show that the geometry of the network of cell-cell junctions reveals important features of the energy landscape associated with the tissue. We use this result to study how local junctional activity controls the viscoelastic properties of the tissue. We find a simple scaling relation between the effective viscosity and the rate of active T1 transformations which is further supported by a coarse-grained theory. Finally, we demonstrate how these active processes significantly affect the global tissue shape by studying the relaxation dynamics of an epithelial tube under axial compression.

II. THE MODEL

We describe epithelial sheets as aggregates of cells under tension. Due to differential adhesion and cortex contractility at the cell-lumen, cell-cell, and cell-substrate interfaces, the effective tensions on apical, basal, and lateral cell sides (Γ_a, Γ_b, and Γ_l, respectively) are all different [33,34]. For the sake of simplicity, we consider tissues where each of these tensions
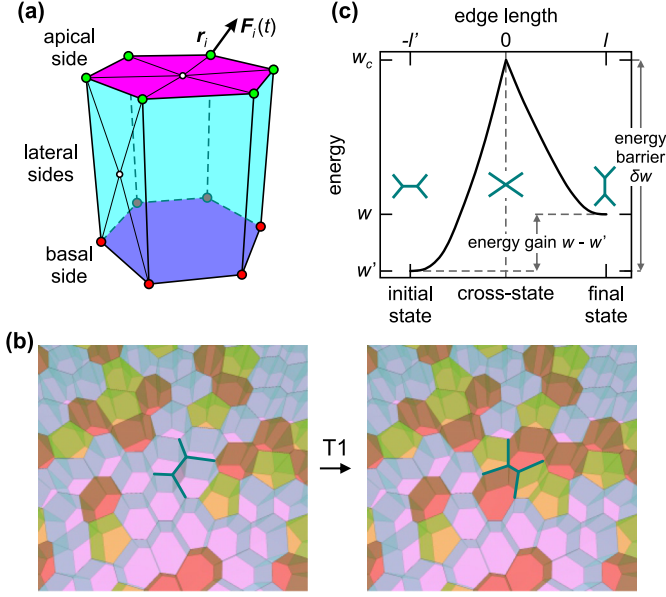
_____
*mkrajnc@princeton.edu

FIG. 1. (a) Schematic of the 3D vertex model. Basal and apical vertices (red and green circles, respectively) move during simulation depending on force $\boldsymbol{F}_i$. (b) Snapshots of a tissue showing a T1 transformation, with the apical sides of 5-, 6-, and 7-coordinated cells in semitransparent yellow, white, and brown, respectively. Edges undergoing the transformation are highlighted. (c) Schematic of tissue energy during a T1 transformation, showing energy barrier $\delta w = w_c - w'$ and energy gain $w - w'$.

is the same in all cells and we choose $\Gamma_a = \Gamma_b = \Gamma$. The shape of each cell is stabilized by an incompressible interior, which imposes a fixed-volume constraint $V_i = V$. We choose $V^{1/3}$ and Γ_l as units of length and tension, respectively, and thus the dimensionless energy measured in units of $\Gamma_l V^{2/3}$ reads

$$w = \sum_{i=1}^{\mathcal{C}} \left[\gamma \left(a_a^{(i)} + a_b^{(i)} \right) + \frac{1}{2} a_l^{(i)} \right], \qquad (1)$$

where $\mathcal{C}$ is the number of cells, $a_a^{(i)}$, $a_b^{(i)}$, and $a_l^{(i)}$ are the dimensionless areas of the apical, basal, and lateral sides of cell i, respectively, and $\gamma = \Gamma/\Gamma_l$ is the dimensionless apical and basal tension; the lateral sides are shared by two cells, hence the factor of $1/2$. The dynamics of cells is given implicitly by the friction-dominated equation of motion for the vertices: $d\boldsymbol{r}_i(t)/dt = \mu_i \boldsymbol{F}_i(t)$. Here $\boldsymbol{r}_i(t)$ is the position of vertex i (Fig. 1(a)), $\mu_i = \mu_0$ is its mobility assumed to be the same in all vertices, and $\boldsymbol{F}_i(t) = -\nabla_i w(\boldsymbol{r}_1, \boldsymbol{r}_2, \boldsymbol{r}_3, \dots)$ is the force on vertex i; $\nabla_i = (\partial/\partial x_i, \partial/\partial y_i, \partial/\partial z_i)$. This equation is solved using a forward finite-difference scheme, the characteristic timescale being $\tau = (\mu_0 \Gamma_l)^{-1}$. For details of implementation, see Sec. I of Supplemental Material [35].

III. ENERGIES OF T1 TRANSFORMATION

The energy landscape of the epithelium is very complex, with each local minimum corresponding to a different in-plane arrangement of cells. The above model dynamics drives the system towards a given minimum, whereas jumping between minima entails topological changes facilitated by T1

transformations [Fig. 1(b)], cell divisions, and cell extrusions [2,12,36–38]. We focus on T1 transformations which are crucial for cell rearrangements and involve four cells around an edge. This edge first shrinks to form a cross-state with a four-way vertex which then dissociates into two three-way vertices, creating a new edge between initially nonneighboring cells [Fig. 1(c)]. The initial and the cross-state are separated by an energy barrier δw which remains finite at any γ unlike in the APE model where it vanishes beyond the rigidity transition [4,8]. Thus, our tissue is intrinsically solid and any cell rearrangement requires an injection of energy via forced topological transformations. In living tissues, these injections come from active contractions of cell cortex driven by the junctional myosin [39,40], the timescale for T1 transformations typically being on the order of minutes to hours [37]. To quantify the impact of active cellular rearrangements, we first study how the two energies associated with a T1 transformation [energy barrier δw and energy gain $w - w'$ defined as the energy difference between the final and the initial state; Fig. 1(c)] depend on network geometry.

We create a 3D cell sheet with a random network of cell-cell junctions by randomly distributing $\mathcal{C} = 340$ points in a 2D square box of size $\mathcal{C} a_0$, where $a_0 = (\sqrt{3}/2)^{1/3}(2\gamma)^{-2/3}$ is the optimal surface area of the cell base (Appendix A). We then construct 2D Voronoi partitions around this set of points and apply periodic boundary conditions on box walls. From the obtained 2D polygonal network we build a 3D tissue and evolve the structure in time so as to satisfy the fixed-volume constraints and to find the minimal-energy structure at the Voronoi-constructed network topology.

We perform T1 transformation on all cell-cell contacts and measure δw and $w - w'$ as functions of $l' = (l_a + l_b)/2$, the average rest length of apical and basal edge of the side in question, for $\gamma = 0.5$, 1, and 2 corresponding to a squamous, a short columnar, and a tall columnar epithelium (Figs. 2(a), 2(b) and 2(c), respectively). By rescaling the energy by $w_0 = 2\gamma^{1/3}/3^{5/6}$ and edge lengths by $l_0 = 3^{-2/3}\gamma^{-1/3}$ (Appendix B), we can almost perfectly collapse the data for both δw and $w - w'$ [Figs. 2(d) and 2(e)]. In particular, we find

$$\delta w = 2\sqrt{3}\gamma R l'^2 \qquad (2)$$

and

$$w - w' = \frac{2\gamma^{2/3} Q}{3^{1/6}} (l' - l^*), \qquad (3)$$

where the fitting parameters $R \approx 0.4$ and $Q \approx 1$, and the threshold length $l^* \approx 0.66 l_0 = 0.66 \times 3^{-2/3}\gamma^{-1/3}$. Moreover, we find the same forms of $\delta w(l')$ and $(w - w')(l')$ in two other mechanical models—the 2D APE model and the 2D foam (Appendix C)—which suggests that relations given by Eqs. (2) and (3) might be generic. This has been recently confirmed in 2D tissue and soap-froth models [41].

To better understand this, we next develop an elastic theory of T1 transformation. Here, the cross state [Fig. 1(c)] can be seen as an elastic deformation of the edge network, described by the shear modulus G (measured in Sec. IV). Elastic energy difference between the cross state and the initial state $\delta w =$
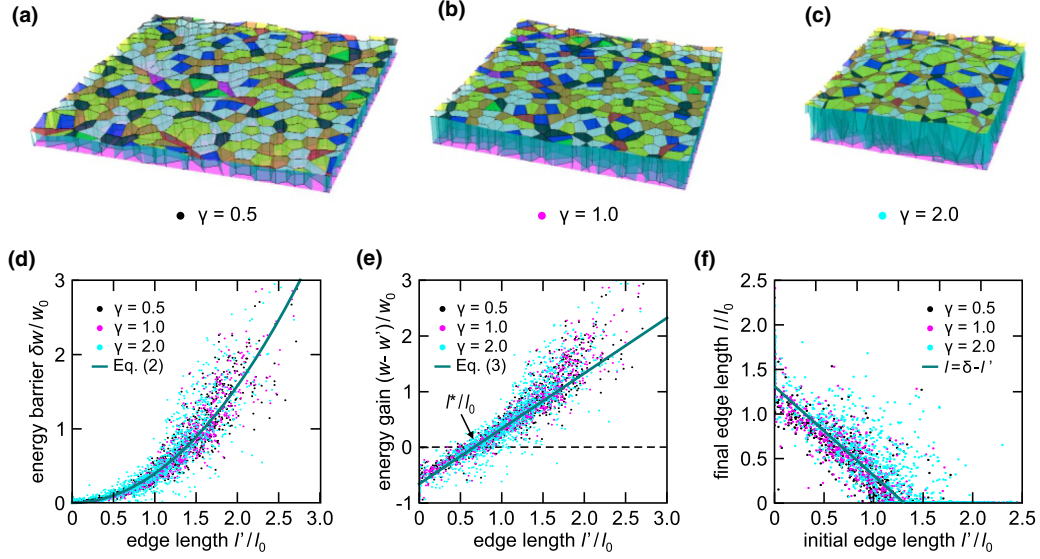
FIG. 2. (a)–(c) Model tissue samples at $\gamma = 0.5$, 1.0, and 2.0 corresponding to a squamous, a short columnar, and a tall columnar tissue, respectively. Note that basal edges can have considerably different lengths than their apical counterparts. This effect is expected due to high degree of disorder, which gives rise to large local variations of the preferred Gaussian curvature—an effect especially prominent in the columnar tissue, e.g., panel (c). Energy barrier $\delta w/w_0$ vs. edge length l'/l_0 (d) and energy gain $(w - w')/w_0$ vs. edge length l'/l_0 (e) for $\gamma = 0.5$, 1, and 2; dots are simulation data and the solid lines are the parabola [Eq. (2)] and the linear function [Eq. (3)]. On average, T1 transformations are preferred below the threshold value $l^*/l_0 \approx 0.66$ (e). (f) Relation between the equilibrium edge length before and after T1 transformation (l' and l, respectively); dots are simulation data and the solid line is the linear function $l = \delta - l'$, where $\delta \approx 1.25l_0$.

$w_c - w'$ reads

$$\delta w = \frac{G}{2} \int dA[(\partial_x u_x - \partial_y u_y)^2 + (\partial_x u_y + \partial_y u_x)^2], \quad (4)$$

where u_x and u_y denote displacements along orthogonal directions. The deformation is obtained by applying a force f_x at $x = l'/2$ and an opposite force $(-f_x)$ at $x = -l'/2$. We neglect a possible residual anisotropy due to finite size of the system and for the sake of simplicity, we assume that the network is incompressible, such that

$$\partial_x u_x + \partial_y u_y = 0 \quad (5)$$

(keeping finite compressibility would not change the final result). Force balance imposes

$$G(\partial_{xx}^2 + \partial_{yy}^2)u_x - \partial_x p = f_x \delta_{x-l'/2} - f_x \delta_{x+l'/2} \quad (6)$$

and

$$G(\partial_{xx}^2 + \partial_{yy}^2)u_y - \partial_y p = 0, \quad (7)$$

where p is pressure and at the boundaries $u_x(\pm l'/2) = \mp l'/2$ and $u_y(\pm l'/2) = 0$. The equations are solved in Fourier space. We obtain

$$u_x\left(\frac{l'}{2}\right) = \frac{f_x}{8\pi G}[\psi - \text{Ci}(q_c l') + \ln(q_c l')] = -\frac{l'}{2}, \quad (8)$$

where we introduced an integration cutoff wave number q_c. In turn, it implies

$$f_x = -\frac{4\pi G}{\psi - \text{Ci}(q_c l') + \ln(q_c l')}l'. \quad (9)$$

Here $\psi = 0.5772156649...$ is the Euler-Mascheroni constant and $\text{Ci}(x) = \psi + \ln x + \int_0^x dt(\cos t - 1)/t$. Now we can calculate the energy barrier δw from its expression in Fourier

space

$$\delta w = \frac{f_x^2}{2\pi^2 G} \int \frac{dq_x}{2\pi} \frac{dq_y}{2\pi} \frac{q_y^2}{(q_x^2 + q_y^2)^2} \sin^2\left(\frac{q_x l'}{2}\right) \quad (10)$$

and obtain

$$\delta w = \frac{2\pi G}{\psi - \text{Ci}(q_c l') + \ln(q_c l')}l'^2. \quad (11)$$

The force needs to vanish when $l' \to 0$, which implies $q_c \propto 1/l'$. Comparing Eq. (11) with Eq. (2) gives $a_c = q_c l' \approx 9.877$, such that $\delta w \propto l'^2$, in agreement with the numerical results.

After the T1 transformation, there exist another equilibrium with energy w. If we apply a force dipole acting along the y direction, we can bring the system to the same cross point with displacement along the y direction. The same calculation as above relates w_c with w with a correction due to the fact that the T1 transformation introduced pairs of pentagons and heptagons:

$$w_c - w = \frac{2\pi G}{\psi - \text{Ci}(a_c) + \ln(a_c)}l^2 + w_{5-7}. \quad (12)$$

We find

$$w - w' = \frac{2\pi G}{\psi - \text{Ci}(a_c) + \ln(a_c)}(l'^2 - l^2) - w_{5-7}, \quad (13)$$

where the relation between l and l' is not known *a priori*. The simulation results show that at lowest order, this relation is linear [Fig. 2(f)]: $l = \delta - l'$, such that, in agreement with simulations,

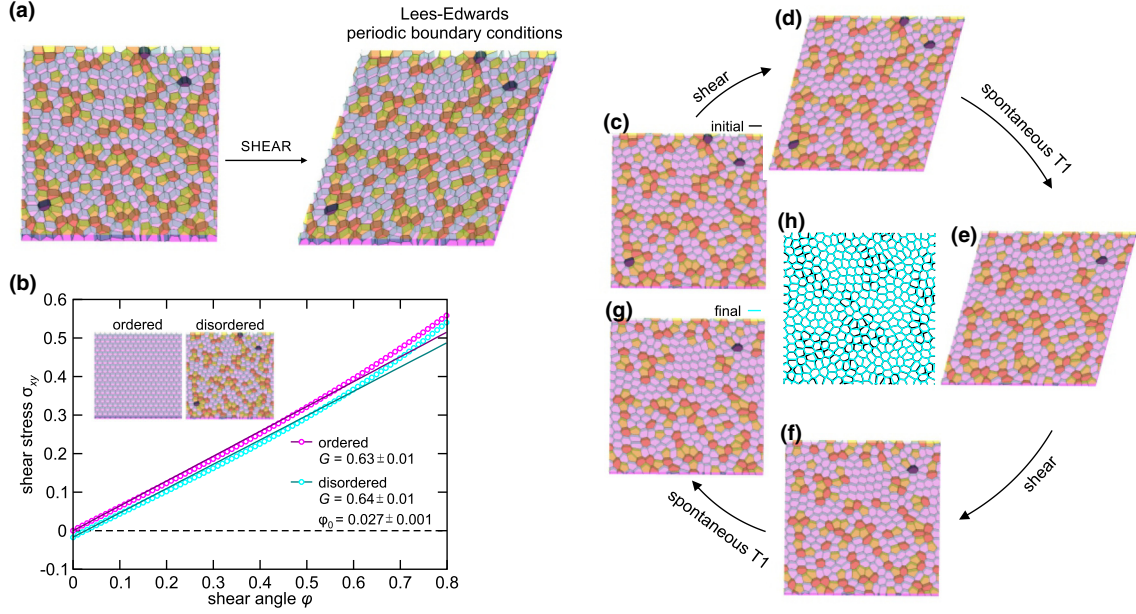$$w - w' = \frac{4\pi G\delta}{\psi - \text{Ci}(a_c) + \ln(a_c)}(l' - l^*), \quad (14)$$

FIG. 3. (a) An example of a partially randomized flat 3D epithelial cell sheet sheared by the use of Lees-Edwards periodic boundary conditions. (b) Shear stress σ_{xy} as a function of shear strain φ for an ordered cell packing (magenta circles) and a disordered cell packing (cyan circles) at $\gamma = 1$. Shear modulus G is extracted from the slope of the linear fit at $\varphi = 0$. (c)–(g) Snapshots of simulations in the direction of arrows show a plastic shear deformation of the tissue. On a short timescale, the tissue is shear-deformed (c), (d) and on a long timescale, it undergoes T1 transformations (d), (e). After applying a reverse shear deformation (e), (f), the tissue deforms back towards the initial shape but the final state (g) is not exactly identical to the initial state because of the irreversible T1 transformations that took place. In the central panel, the initial and the final edge networks (black and cyan edges, respectively) are compared (h).

where the threshold length

$$l^* = \frac{\delta}{2} + \frac{w_{5-7}[\psi - \mathrm{Ci}(a_c) + \ln(a_c)]}{4\pi G \delta}. \quad (15)$$

Comparing Eqs. (14) and (3) gives $\delta/l_0 = 1.25$, which again agrees with simulations [Fig. 2(f)]. These results further confirm that the relations given by Eqs. (2) and (3) are not specific to our model.

IV. ACTIVE T1 TRANSFORMATIONS

The above results allow us to efficiently simulate random T1 transformations driven by junctional activity. To this end, we adapt the standard Metropolis algorithm such that the uphill active transformations on edges longer than l^* take place with a finite probability independent of the rest length l', whereas the probability of their downhill spontaneous counterparts on edges shorter than l^* is 1 as usual. In particular, the probability for the former is given by $k_{\mathrm{T1}}\delta t/\mathcal{E}$, where $\mathcal{E}$ is the number of edges, $\delta t = 0.001$ is the time step, and k_{T1} is the rate of active T1 transformations measured in units of $1/\tau$. Within the simplest nonequilibrium scheme, the imposed active noise is large compared to the barrier height and so the T1 rate does not explicitly depend the height of the energy barrier.

To quantify the viscoelastic response, we compute the stress caused by a sudden in-plane simple-shear strain in a slightly disordered $\gamma = 1$ tissue with $\mathcal{C} = 340$ cells and $\mathcal{E} = 1020$ edges [Fig. 3(a)]. In units of $\Gamma_l V^{-1/3}$, the xy component of the stress reads

$$\sigma_{xy} = -\frac{1}{\mathcal{C}} \sum_{m \in \text{lateral sides}} n_x^{(m)} n_y^{(m)} a_m, \quad (16)$$

where a_m is the area of lateral side m, whereas $n_x^{(m)}$ and $n_y^{(m)}$ are the components of its normal [42].

A short-time or small-deformation response to a simple-shear deformation is elastic. The timescale associated with the elastic behavior is much shorter than the timescale for T1 transformations $1/k_{\mathrm{T1}}$. Thus, the tissue deforms at a fixed network topology and is able to relax back to the initial state when the reverse deformation is applied. In the linear regime, shear stress σ_{xy} is proportional to shear strain φ:

$$\sigma_{xy} = G\varphi, \quad (17)$$

where the proportionality coefficient is the shear modulus G. We extract G from simulations of a quasi-static shear deformation of the $\gamma = 1$ tissue by calculating the slope of the $\sigma_{xy}(\varphi)$ curve: $G = (d\sigma_{xy}/d\varphi)|_{\varphi=0}$. Figure 3(b) shows σ_{xy} as a function of the shear angle φ. In both ordered and disordered case, the linear regime extends to $\varphi \approx 0.5$. As expected, the shear modulus G does not depend on the in-plane structure of the tissue. However, topology does influence the preferred shear angle φ_0 which is equal to zero in the ordered tissue and generally nonzero albeit very small in disordered tissues.

For moderate to large deformations at short times, the tissue undergoes a plastic deformation. This happens due to spontaneous T1 transformations, which change the topology of the tissue so that after strain is removed the tissue cannot spontaneously relax back to the initial configuration [Fig. 3(c)–3(h)]. Similarly to soap froths, which may be viewed as a passive analog of tissues, the spontaneous T1 transformations partially reduce the overall stress, yet the tissue still behaves like a solid for any chosen values of
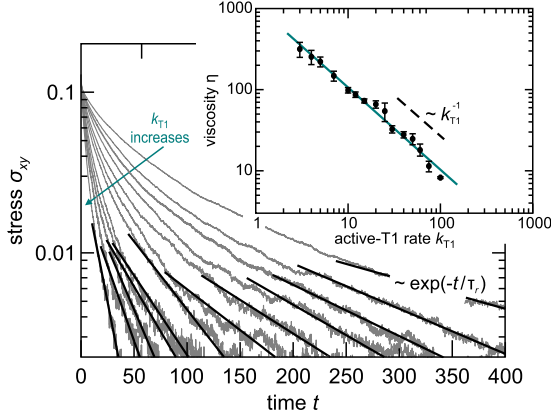
FIG. 4. Stress-relaxation curves for $k_{T1} = 7, 10, 12, 15, 20, 25, 30, 40, 50, 60, 75$, and 100 (top to bottom). The short-time elastic regime terminates at t smaller than about $1/7, 1/10, ..., 1/100$, respectively. In the long-time viscous regime, stress decays exponentially; the relaxation time τ_r is obtained from fits (solid lines). Error bars were estimated by varying the fitting intervals. Inset: Viscosity η vs. active-T1 rate k_{T1}.

model parameters and therefore cells cannot rearrange so as to completely relax the stress.

At long times, the stress decays to zero, which indicates a viscous response. In particular, $\sigma_{xy} \propto \exp(-t/\tau_r)$ where τ_r is the relaxation time, which is computed by fitting the stress-relaxation data averaged over 500 simulation runs (Fig. 4). The obtained τ_r are then used to estimate the tissue viscosity η using the relation $\eta = G\tau_r$ and study its dependence on the active-T1 rate. We find that η rapidly decreases with k_{T1} and that

$$\eta \propto k_{T1}^{-1}, \tag{18}$$

as shown in the inset to Fig. 4.

To better understand this result, we develop a coarse-grained theory, using the approach described in Ref. [14]. We write the stress as $\sigma_{ij} = \sigma\delta_{ij} + \widetilde{\sigma}_{ij}$, where σ and $\widetilde{\sigma}_{ij}$ are its isotropic and traceless part, respectively. The rate of change of traceless stress $\widetilde{\sigma}_{ij}$ can be expressed as the sum of the elastic term and the source term due to active T1 transformations dressed by any subsequent rearrangements:

$$\frac{D\widetilde{\sigma}_{ij}}{Dt} = 2G\widetilde{v}_{ij} + \widetilde{\Pi}_{ij}. \tag{19}$$

Here $v_{ij} = (\partial_i v_j + \partial_j v_i)/2$ is the strain rate tensor and $\widetilde{v}_{ij}$ is its traceless part, $\widetilde{\Pi}_{ij}$ is the stress source, and $D\widetilde{\sigma}_{ij}/Dt = \partial_t\widetilde{\sigma}_{ij} + v_k\partial_k\widetilde{\sigma}_{ij} + \omega_{ik}\widetilde{\sigma}_{kj} + \omega_{jk}\widetilde{\sigma}_{ik}$ is the convected corotational time derivative, $\omega_{ij} = (\partial_i v_j - \partial_j v_i)/2$ being the vorticity of the flow.

When the individual dressed active T1 transformations do not interact with each other, the source term $\widetilde{\Pi}_{ij} = k_{T1}\widetilde{r}_{ij}$, where $\widetilde{r}_{ij}$ denotes the stress generated by one such event. In absence of stress, the average $\langle\widetilde{r}_{ij}\rangle$ must vanish on symmetry grounds both in the disordered and in the ordered tissues with infinite and six-fold rotational symmetry, respectively, even though each event provides a stress source. The presence of stress introduces a bias so that both $\langle\widetilde{\sigma}_{ij}\rangle$ and $\langle\widetilde{r}_{ij}\rangle$ are nonzero.

As the dressed active T1 transformations reduce the stress,

$$\langle\widetilde{r}_{ij}\rangle = -\alpha\langle\widetilde{\sigma}_{ij}\rangle, \tag{20}$$

where α is a dimensionless coefficient which measures the efficiency of the process. Thus, $\langle\widetilde{\Pi}_{ij}\rangle = -k_{T1}\alpha\langle\widetilde{\sigma}_{ij}\rangle$ and after averaging and rearranging Eq. (19) we obtain the Maxwell constitutive relation

$$\langle\widetilde{\sigma}_{ij}\rangle + \tau_M\left\langle\frac{D\widetilde{\sigma}_{ij}}{Dt}\right\rangle = 2\eta\langle\widetilde{v}_{ij}\rangle, \tag{21}$$

where $\tau_M = 1/(k_{T1}\alpha)$ is the relaxation time and $\eta = \tau_M G$, which immediately gives $\eta = (G/\alpha)k_{T1}^{-1}$ just like in the vertex model [where the dimensionless coefficient $\alpha = 5.8 \times 10^{-4}$ (Fig. 4)]. This allows us to conclude that at long times where $D\widetilde{\sigma}_{ij}/Dt$ vanishes and $\langle\widetilde{\sigma}_{ij}\rangle = 2\eta\langle\widetilde{v}_{ij}\rangle$, the epithelium can be treated as a viscous fluid. Equation (21) introduces a single relaxation time. A more refined analysis leading to a distribution of these times is given in Appendix D; τ_M is related to this distribution via Eq. (D6).

V. 3D TISSUE SHAPE

We now employ our model to demonstrate how the active T1 transformations affect the overall 3D shape of the tissue, examining the interplay of shape and structure in an axially compressed epithelial tube of $\mathcal{C} = 336$ cells [Fig. 5(a)]. Starting from an ordered state where all cells are 6-coordinated, we deform the tube at a constant compression rate $\Delta L/\tau_C = 7 \times 10^{-3}$, where $\tau_C = 500$ is the time in which the tube is compressed by 30%, and at three different active-T1 rates k_{T1}. At a small $k_{T1} = 3$, the tube is essentially elastic and buckles beyond the critical compressive strain [Figs. 5(b) and 5(h)]. At $k_{T1} = 20$, the relaxation time τ_M is shorter but of the same order than τ_C and cells partially rearrange upon compression, which makes the tube smoother [Fig. 5(c)]. The $k_{T1} = 100$ case [Fig. 5(d)] corresponds to an extremely active tissue which readily flows while compressed, thereby avoiding buckling and merely transforming into a shorter tube with a larger diameter. Figures 5(e)–5(g) quantify the deviation of shapes in Figs. 5(b)–5(d) from the cylinder in terms of radial modulation $\Delta r = r/\langle r\rangle - 1$, where r is the distance of a cell centroid from the axis and and $\langle r\rangle$ is its average over all cells. Here Δr is plotted in the (z, ϕ) plane, where z is the lengthwise coordinate and ϕ is the polar angle. The evolution of these shapes is shown in the Supplemental Material, Movies M1–M3 [35].

The in-plane structure of the tube is closely related to its 3D shape. In Figs. 5(h)–5(j) we plot the degree of disorder D (defined by $1 - \nu_6$ where ν_6 is the frequency of 6-coordinated cells) and the average magnitude of Δr against relative compression. In the $k_{T1} = 3$ and 20 tubes, the tissue remains ordered as long as it does not buckle. This is because the bound 4-cell pair of dislocations created by an active T1 transformation undergoes a reverse transformation before these cells can interact with other non-6-coordinated cells [Figs. 5(h) and 5(i)]. Close to the buckling instability, more and more dislocations as well as disclinations survive so as to relax the stress and disorder is increased. In the fluidized tissue with $k_{T1} = 100$, the density of such defects quickly saturates and so does the value of D [Fig. 5(j)]. This leads to a steady-state packing with a well-defined distribution of polygonal classes.
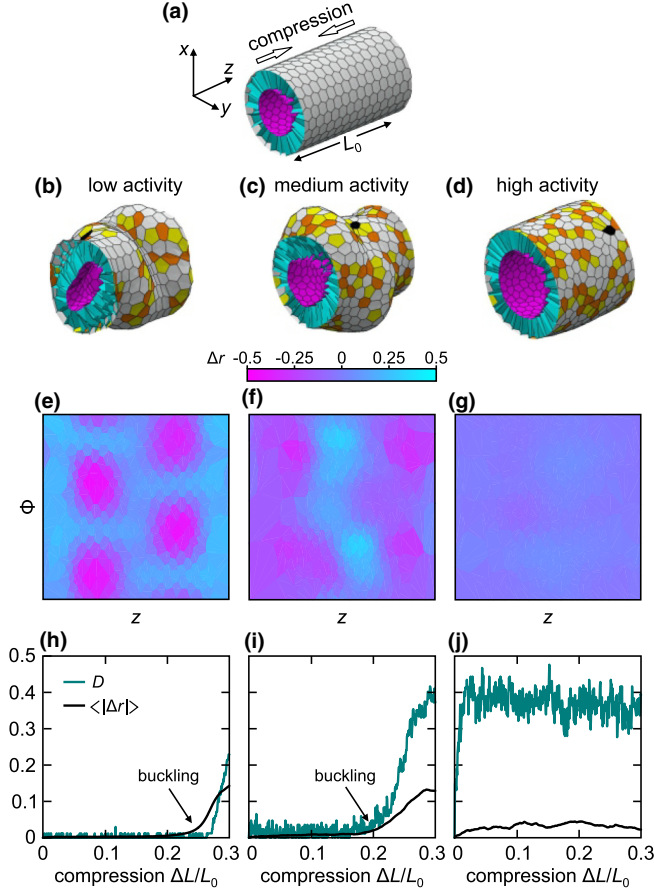
(a) compression L_0

(b) low activity **(c)** medium activity **(d)** high activity

Δr -0.5 -0.25 0 0.25 0.5

(e) **(f)** **(g)**

Φ

z z z

(h) **(i)** **(j)**

compression $\Delta L/L_0$ compression $\Delta L/L_0$ compression $\Delta L/L_0$

FIG. 5. Epithelial tube before (a) and after axial compression by $\Delta L/L_0 = 0.3$ at $k_{\text{T1}} = 3$, 20, and 100 (b), (c), and (d), respectively); the color-coded deformation patterns encoded by radial modulation Δr are shown in panels (e)–(g). Average magnitude of radial modulation $\langle|\Delta r|\rangle$ and disorder D vs. relative compression at $k_{\text{T1}} = 3$, 20, and 100 (h), (i), and (j), respectively).

VI. CONCLUSIONS

The main novelty of our dynamical 3D vertex model of epithelia is the concept of tissue fluidization due to active noise at cell-cell junctions, which regulates the stress-relaxation timescale. This represents a new mechanism involved in the rigidity transition in tissues [17], which does not rely on vanishing energy barriers and is thus independent on the choice of the work function.

Our implementation of the active noise is based on exploration of the tissue energy landscape by forced neighbor exchanges. We showed that the geometry of the junctional network encodes some of the local features of this landscape. In particular, we discovered relations between the lengths of cell-cell junctions and energies involved in a T1 transformation. Using an elastic theory, we showed that these relations should not depend on the choice of the model-energy functional.

Furthermore, devoid of simplifications immanent to its 2D analogs, our model can be used to explore the interplay of activity, in-plane structure, and 3D shape of tissues in various contexts, especially when generalized by including cell division and extrusion—to, e.g., describe the form of villi and crypts in the intestinal epithelium (Sec. II of Supplemental Material [35]). An important application will be a study of early embryonic development, say in *Drosophila*, which will allow one to comprehensively explore the mechanics of the morphogenetic events involved. Here active T1 transformations may be biased by tissue in-plane polarization [43] and their rate (and thus the degree of fluidization) may vary between the different parts of the embryo. Finally, when further developed, our approach may be useful in finding robust ways to engineer tissues with different shapes and functionalities *in vitro*, e.g., organoids.

APPENDIX A: 3D TENSION-BASED MODEL

We treat epithelial cell sheets as aggregates of incompressible cells carrying differential surface tensions at the apical, basal, and lateral cell sides (Γ_a, Γ_b, and Γ_l, respectively) [44–47], such that the total mechanical energy of a cell reads

$$W = \Gamma_a A_a + \Gamma_b A_b + \tfrac{1}{2}\Gamma_l A_l, \tag{A1}$$

where A_a, A_b, and A_l are the surface areas of the apical, basal, and lateral cell sides. Due to incompressibility, cell volume is fixed ($V = \text{const.}$). For simplicity, we assume that all tensions are positive (Γ_a, Γ_b, $\Gamma_l > 0$) which is true in the limit where the cortical tension is dominant over the adhesion strength. Let us describe cells as prisms with regular polygonal base. For a hexagonal base $A_a = A_b \equiv A$, $A_l = 2h\sqrt{2\sqrt{3}A}$, and $V = Ah = \text{const.} = 1$, where A is the surface area of the base and h is the cell height. In dimensionless form where the dimensionless apical tension $\alpha = \Gamma_a/\Gamma_l$ and the dimensionless basal tension $\beta = \Gamma_b/\Gamma_l$, $a = A/V^{2/3}$, and $w = W/(V^{2/3}\Gamma_l)$, the total energy [Eq. (A1)] of a cell reads

$$w = (\alpha + \beta)a + \frac{\sqrt{2\sqrt{3}}}{\sqrt{a}}. \tag{A2}$$

The equilibrium surface area of the cell base a_0 is calculated from the force balance equation ($\partial w/\partial a = \alpha + \beta - \sqrt{\sqrt{3}/2a^3} = 0$) and reads

$$a_0 = \left(\frac{\sqrt{3}}{2}\right)^{1/3}(\alpha + \beta)^{-2/3}, \tag{A3}$$

whereas the equilibrium cell height h_0 is calculated from the fixed-volume constraint $h_0 = 1/a_0$:

$$h_0 = \left(\frac{\sqrt{3}}{2}\right)^{-1/3}(\alpha + \beta)^{2/3}. \tag{A4}$$

By combining Eqs. (A2) and (A3), we obtain the equilibrium cell energy $w_0 = 3[\sqrt{3}(\alpha + \beta)/2]^{1/3}$. In a flat geometry, the ground state corresponds to a tissue where cells of height h_0 and cell-base area a_0 are packed in a regular hexagonal lattice with 6-coordinated cells.

The most basic classification of epithelial monolayers relies on their width-to-height ratio $\Phi = d/h$, where d is the cell diameter. The preferred cell width-to-height ratio, defined as $\Phi_0 = d_0/h_0$ where $d_0 = \sqrt{2a_0/\sqrt{3}}$, reads

$$\Phi_0 = \frac{1}{\alpha + \beta}. \tag{A5}$$

For $\alpha + \beta < 1$ the tissue is squamous ($d/h > 1$), for $\alpha + \beta > 1$ the tissue is columnar ($d/h < 1$), whereas for $\alpha + \beta \approx 1$ the tissue is cuboidal ($d/h \approx 1$).

Generally, tissue can spontaneously fold due to apicobasal polarity [27], which can be modeled by a nonzero apicobasal differential tension ($\alpha - \beta \neq 0$). Here we do not consider such a case and thus we assume that $\alpha = \beta \equiv \gamma$.

APPENDIX B: COLLAPSE OF DATA FOR δw AND $w - w'$

Let us denote the surface area of the midplane of cell i by $a_i \approx [a_a^{(i)} + a_b^{(i)}]/2$, such that the total energy of the system [Eq. (1)] simplifies to

$$w = \sum_{i=1}^{\mathcal{C}} \left[2\gamma a_i + \frac{1}{2} a_l^{(i)} \right], \tag{B1}$$

where $a_l^{(i)} \approx p_i h_i$ is the total lateral area of cell i (p_i being the perimeter of the midplane). Assuming that cell height is uniform across the tissue (i.e., $h_i = h_0 = 2 \cdot 3^{-1/6} \gamma^{2/3}$) and that the volumes of all cells are fixed, we can write $a_i \approx 1/h_0$ for all i so that the total energy

$$w = \frac{2\mathcal{C}\gamma}{h_0} + \frac{h_0}{2} \sum_{i=1}^{\mathcal{C}} p_i. \tag{B2}$$

This can be further simplified by rewriting the sum over all cells as a sum over all edges such that

$$w = \frac{2\mathcal{C}\gamma}{h_0} + h_0 \sum_{i=1}^{\mathcal{E}} l_i = \text{const.} + h_0 \sum_{i=1}^{\mathcal{E}} l_i. \tag{B3}$$

This result suggests that it might be possible to collapse the data for δw and $w - w'$ [Eqs. (2) and (3), respectively] by rescaling the energy by $h_0 l_0$ and the edge length by l_0, where $l_0 = 3^{-2/3} \gamma^{-1/3}$ is the lattice constant of the corresponding ground-state honeycomb lattice. Thus, the rescaled energy barrier

$$\frac{\delta w}{h_0 l_0} = R \left(\frac{l'}{l_0} \right)^2, \tag{B4}$$

whereas the rescaled energy gain

$$\frac{w' - w}{h_0 l_0} = Q \left(\frac{l'}{l_0} - \frac{l^*}{l_0} \right). \tag{B5}$$
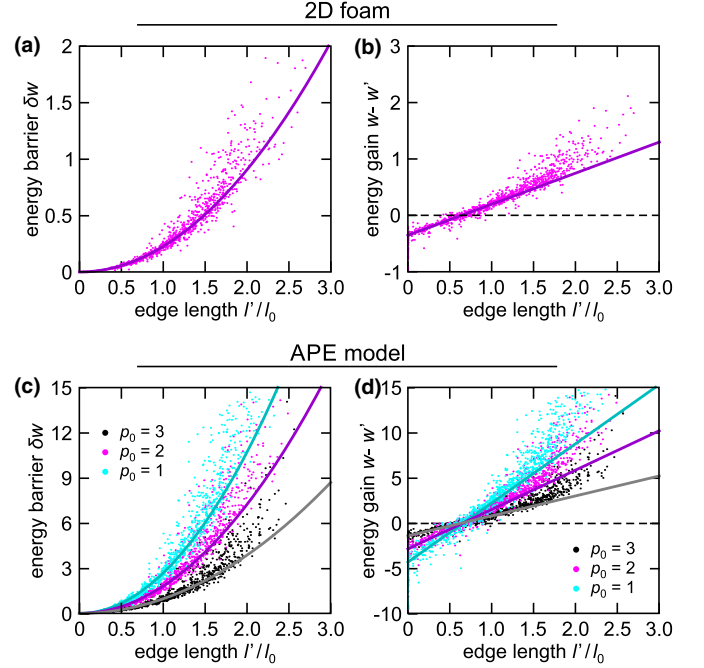

FIG. 6. Energy barrier $\delta w/w_0$ vs. edge length l'/l_0 (a), (c) and energy gain $(w - w')/w_0$ vs. edge length l'/l_0 (b), (d) for the 2D-foam model and the 2D APE model, respectively. Dots are simulation data and the solid lines are Eqs. (2) and (3), respectively. The threshold value $l^*/l_0 \approx 0.64$ and 0.66 (panels (b) and (d), respectively).

APPENDIX C: COMPARISON TO APE MODEL AND 2D SOAP FROTH

To test whether the obtained relationships $\delta w(l')$ and $(w - w')(l')$ hold for other tissue model-energy functionals as well, we perform the analysis of energy barriers and energy gains for two other mechanical models: 2D foam model and the APE model. We consider a planar polygonal tiling of straight edges. The model dimensionless energy in the 2D foam

$$w_{\text{2Dfoam}} = \sum_{i=1}^{\mathcal{E}} l_i + k_A \sum_{i=1}^{\mathcal{C}} (a_i - 1)^2, \tag{C1}$$

whereas in the APE model

$$w_{\text{APE}} = \sum_{i=1}^{\mathcal{C}} (p_i - p_0)^2 + k_A \sum_{i=1}^{\mathcal{C}} (a_i - 1)^2, \tag{C2}$$

where p_0 is the preferred perimeter of cells. In both models we assume that the cells are nearly incompressible and set $k_A = 100$.

We construct a random tiling of cells using the Voronoi construction and perform T1 transformation on all edges just like in the 3D tension-based model (Fig. 2). We measure δw and $w - w'$ and plot them versus the initial edge rest length l' (Fig. 6). The 2D-foam model has no free parameters, whereas for the APE model, we plot δw and $w - w'$ for three values of the preferred perimeter $p_0 = 1, 2,$ and 3 (all corresponding to the solid-tissue regime). We find that just like in the 3D tension-based model, $\delta w \propto l'^2$ and $w - w' \propto l' - l^*$. Furthermore, the threshold length in both 2D foam and in 2D APE model agrees very well with that of the 3D tension-based model. In

particular, we find $l^*_{\text{2Dfoam}} \approx 0.64 l_0$ and $l^*_{\text{APE}} \approx 0.66 l_0$, where $l_0 = \sqrt{2}/3^{3/4}$ is the lattice constant of the lattice of unit-area regular hexagons [Figs. 6(b) and 6(d)].

APPENDIX D: NONEXPONENTIAL STRESS RELAXATION

We start from the relation between the stress derivative, the strain rate, and the stress sources due to imposed T1 transformations and subsequent relaxation as introduced in the main text:

$$\frac{D\widetilde{\sigma}_{ij}}{Dt} = 2G\widetilde{v}_{ij} + \widetilde{\Pi}_{ij}. \quad \text{(D1)}$$

The stress source $\widetilde{\Pi}_{ij} = k_{\text{T1}}\langle \widetilde{r}_{ij} \rangle$ is the sum of all stresses corresponding to pairs of forced T1/relaxations events. Each pair of events has its own timescale and amplitude and the relation $\langle \widetilde{r}_{ij} \rangle = -\alpha \langle \widetilde{\sigma}_{ij} \rangle$ used in a mean-field approach, valid only at long times. Here we elaborate this simple mean-field description by assuming that each pair of events is characterized by an initial edge length l'. (In principle, it also depends on the the orientation of the edge in question, cell connectivity, etc.) Keeping just the edge length dependence is again a simplification but it allows us to understand the nonexponential relaxation observed in the simulations in a simple way.

The relation between the average source stress and that of events with initial edge length l' is given by

$$\langle \widetilde{r}_{ij} \rangle = \int_0^{l'_{\text{max}}} dl' P_{l'} \langle \widetilde{r}^{l'}_{ij} \rangle, \quad \text{(D2)}$$

where P_l is the edge length probability distribution and $\langle \widetilde{r}^{l'}_{ij} \rangle$ is the average stress source corresponding to events with initial edge length l'. Here l'_{max} is the maximal possible edge length. The dynamics of such events can be characterized by a time $\tau_{l'}$ and an amplitude $\chi_{l'}$ such that in the linear regime,

$$\tau_{l'} \frac{\partial \langle \widetilde{r}^{l'}_{ij} \rangle}{\partial t} + \langle \widetilde{r}^{l'}_{ij} \rangle = -\chi_{l'} \langle \widetilde{\sigma}_{ij} \rangle, \quad \text{(D3)}$$

or after integration,

$$\langle \widetilde{r}^{l'}_{ij}(t) \rangle = -\frac{\chi_{l'}}{\tau_{l'}} \int_0^t \exp\left(-\frac{t-s}{\tau_{l'}}\right) \langle \widetilde{\sigma}_{ij}(s) \rangle ds. \quad \text{(D4)}$$

Now the stress evolution equation reads

$$\frac{D\widetilde{\sigma}_{ij}}{Dt} = 2G\widetilde{v}_{ij} - k_{\text{T1}} \int_0^t ds \int_0^{l'_{\text{max}}} dl' \frac{P^{ss}_{l'} \chi_{l'}}{\tau_{l'}}$$

$$\times \exp\left(-\frac{t-s}{\tau_{l'}}\right) \widetilde{\sigma}_{ij}(s). \quad \text{(D5)}$$

For long enough times or for slow enough stress variations, one recovers the Maxwell relation in the main text [Eq. (7) of the main text] with

$$\tau_M^{-1} = k_{\text{T1}} \int_0^{l'_{\text{max}}} dl' P_{l'} \chi_{l'}. \quad \text{(D6)}$$

However, note that Eq. (D5) involves a continuum of timescales as observed in the simulation. This is particularly clear in the Fourier space, where the linearized relation between stress and strain now reads

$$\left(i\omega + k_{\text{T1}} \int_0^{l'_{\text{max}}} \frac{dl' P_{l'} \chi_{l'}}{1 + \omega^2 \tau_{l'}^2}\right) \langle \widetilde{\sigma}_{ij}(\omega) \rangle = 2G\widetilde{v}_{ij}(\omega). \quad \text{(D7)}$$

[1] M. Rauzi, U. Krzic, T. E. Saunders, M. Krajnc, P. Ziherl, L. Hufnagel, and M. Leptin, Nat. Commun. **6**, 8677 (2015).

[2] R. Etournay, M. Popovic, M. Merkel, A. Nandi, C. Blasse, B. Aigouy, H. Brandl, G. Myers, G. Salbreux, F. Jülicher, and S. Eaton, eLife **4**, e07090 (2015).

[3] D. Bi, J. H. Lopez, J. M. Schwarz, and M. L. Manning, Soft Matter **10**, 1885 (2014).

[4] D. Bi, J. Lopez, J. Schwarz, and M. L. Manning, Nat. Phys. **11**, 1074 (2015).

[5] T. E. Angelini, E. Hannezo, X. Trepat, M. Marquez, J. J. Fredberg, and D. A. Weitz, Proc. Natl. Acad. Sci. USA **108**, 4714 (2011).

[6] E.-M. Shoetz, M. Lanio, J. A. Talbot, and M. L. Manning, J. R. Soc. Interface **10**, 20130726 (2013).

[7] L. Berthier and G. Biroli, Rev. Mod. Phys. **83**, 587 (2011).

[8] R. Farhadifar, J.-C. Röper, B. Aigouy, S. Eaton, and F. Jülicher, Curr. Biol. **17**, 2095 (2007).

[9] L. Hufnagel, A. A. Teleman, H. Rouault, S. M. Cohen, and B. I. Shraiman, Proc. Natl. Acad. Sci. USA **104**, 3835 (2007).

[10] K. D. Irvine and E. Wieschaus, Development **120**, 827 (1994).

[11] R. Keller, Development **133**, 2291 (2006).

[12] M. Rauzi, P. F. Lenne, and T. Lecuit, Nature **468**, 1110 (2010).

[13] M. Popović, A. Nandi, M. Merkel, R. Etournay, S. Eaton, F. Jülicher, and G. Salbreux, New J. Phys. **19**, 033006 (2017).

[14] J. Ranft, M. Basan, J. Elgeti, J. F. Joanny, J. Prost, and F. Jülicher, Proc. Natl. Acad. Sci. USA **107**, 20863 (2010).

[15] D. A. Matoz-Fernandez, K. Martens, R. Sknepnek, J.-L. Barrat, and S. Henkes, Soft Matter **13**, 3205 (2017).

[16] D. A. Matoz-Fernandez, E. Agoritsas, J.-L. Barrat, E. Bertin, and K. Martens, Phys. Rev. Lett. **118**, 158105 (2017).

[17] D. Bi, X. Yang, M. C. Marchetti, and M. L. Manning, Phys. Rev. X **6**, 021011 (2016).

[18] X. Yang, D. Bi, M. Czajkowski, M. Merkel, M. L. Manning, and M. C. Marchetti, Proc. Natl. Acad. Sci. USA **114**, 12663 (2017).

[19] D. L. Barton, S. Henkes, C. J. Weijer, and R. Sknepnek, PLoS Comp. Biol. **13**, e1005569 (2017).

[20] A. Hočevar and P. Ziherl, Phys. Rev. E **80**, 011904 (2009).

[21] D. B. Staple, R. Farhadifar, J.-C. Röper, B. Audoly, S. Eaton, and F. Jülicher, Eur. Phys. J. E **33**, 117 (2010).

[22] M. Osterfield, X. Du, T. Schüpbach, E. Wieschaus, and S. Y. Shvartsman, Dev. Cell **24**, 400 (2013).

[23] A. G. Fletcher, M. Osterfield, R. E. Baker, and S. Y. Shvartsman, Biophys. J. **106**, 2291 (2014).

[24] N. Murisic, V. Hakim, I. G. Kevrekidis, S. Y. Shvartsman, and B. Audoly, Biophys. J. **109**, 154 (2015).

[25] B. Monier, M. Gettings, G. Gay, T. Mangeat, S. Schott, A. Guarner, and M. Suzanne, Nature **518**, 245 (2015).

[26] A. Hočevar Brezavšček, M. Rauzi, M. Leptin, and P. Ziherl, Biophys. J. **103**, 1069 (2012).

[27] M. Krajnc and P. Ziherl, Phys. Rev. E **92**, 052713 (2015).

[28] N. Štorgel, M. Krajnc, P. Mrak, J. Štrus, and P. Ziherl, Biophys. J. **110**, 269 (2016).

[29] S. Okuda, Y. Inoue, M. Eiraku, T. Adachi, and Y. Sasai, Biomech. Model Mechanobiol. **14**, 413 (2015).

[30] C. Bielmeier, S. Alt, V. Weichselberger, M. La Fortezza, H. Harz, F. Jülicher, G. Salbreux, and A. K. Classen, Curr. Biol. **26**, 563 (2016).

[31] M. Misra, B. Audoly, I. G. Kevrekidis, and S. Y. Shvartsman, Biophys. J. **110**, 1670 (2016).

[32] S. Alt, P. Ganguly, and G. Salbreux, Philos. Trans. R. Soc. B **372**, 20150520 (2017).

[33] J. A. Glazier and F. Graner, Phys. Rev. E **47**, 2128 (1993).

[34] E. Hannezo, J. Prost, and J. F. Joanny, Proc. Natl. Acad. Sci. USA **111**, 27 (2014).

[35] See Supplemental Material at http://link.aps.org/supplemental/10.1103/PhysRevE.98.022409 for supporting calculations and figures.

[36] E. Marinari, A. Mehonic, S. Curran, J. Gale, T. Duke, and B. Baum, Nature **484**, 542 (2012).

[37] T. Wyatt, B. Baum, and G. Charras, Curr. Opin. Cell Biol. **38**, 68 (2016).

[38] S. A. Gudipaty, J. Lindblom, P. D. Loftys, M. J. Reed, K. Edes, C. F. Davey, V. Krishnegowda, and J. Rosenblatt, Nature **543**, 118 (2017).

[39] S. Curran, C. Strandkvist, J. Bathmann, M. de Gennes, A. Kabla, G. Salbreux, and B. Baum, Dev. Cell **43**, 480 (2017).

[40] J. Prost, F. Jülicher, and J.-F. Joanny, Nat. Phys. **11**, 111 (2015).

[41] S. Kim, Y. Wang, and S. Hilgenfeldt, Phys. Rev. Lett. **120**, 248001 (2018).

[42] G. K. Batchelor, J. Fluid Mech. **41**, 545 (1970).

[43] C. Collinet. M. Rauzi, P.-F. Lenne, and T. Lecuit, Nat. Cell Biol. **17**, 1247 (2015).

[44] D. W. Thompson, *On Growth and Form* (Cambridge University Press, Cambridge, 1917).

[45] M. S. Steinberg, Science **141**, 401 (1963).

[46] A. K. Harris, J. Theor. Biol. **61**, 267 (1976).

[47] J. Derganc, S. Svetina, and B. Žekš, J. Theor. Biol. **260**, 333 (2009).